Zhang and Sagiya *Earth, Planets and Space* (2017) 69:82
DOI 10.1186/s40623-017-0668-5

Earth, Planets and Space

FULL PAPER Open Access

Shear strain concentration mechanism in the lower crust below an intraplate strike-slip fault based on rheological laws of rocks

Xuelei Zhang[1*] and Takeshi Sagiya[2]

Abstract

We conduct a two-dimensional numerical experiment on the lower crust under an intraplate strike-slip fault based on laboratory-derived power-law rheologies considering the effects of grain size and water. To understand the effects of far-field loading and material properties on the deformation of the lower crust on a geological time scale, we assume steady fault sliding on the fault in the upper crust and ductile flow for the lower crust. To avoid the stress singularity, we introduce a yield threshold in the brittle–ductile transition near the down-dip edge of the fault. Regarding the physical mechanisms for shear strain concentration in the lower crust, we consider frictional and shear heating, grain size, and power-law creep. We evaluate the significance of these mechanisms in the formation of the shear zone under an intraplate strike-slip fault with slow deformation. The results show that in the lower crust, plastic deformation is possible only when the stress or temperature is sufficiently high. At a similar stress level, ~100 MPa, dry anorthite begins to undergo plastic deformation at a depth around 28–29 km, which is about 8 km deeper than wet anorthite. As a result of dynamic recrystallization and grain growth, the grain size in the lower crust may vary laterally and as a function of depth. A comparison of the results with constant and non-constant grain sizes reveals that the shear zone in the lower crust is created by power-law creep and is maintained by dynamically recrystallized material in the shear zone because grain growth occurs in a timescale much longer than the recurrence interval of intraplate earthquakes. Owing to the slow slip rate, shear and frictional heating have negligible effects on the deformation of the shear zone. The heat production rate depends weakly on the rock rheology; the maximum temperature increase over 3 Myr is only about several tens of degrees.

Keywords: Intraplate strike-slip fault, 2-D thermal-mechanical fault model, Ductile shear zone

Introduction

Ductile shear zones are believed to exist in the lower crust below interplate strike-slip faults on the basis of various observational, experimental, and theoretical studies as well as geological observations of exhumed shear zones. Thermal weakening due to shear heating has been considered as an important process for the development and maintenance of shear zones (e.g., Yuen et al. 1978; Fleitout and Froidevaux 1980). Observation of the broadly distributed heat flow anomaly on the San Andreas Fault (see Lachenbruch and Sass 1980) has been explained by shear heating in the lower crust. The temperature anomaly in the lower crust can reach several hundred degrees, which can create an observable heat flow anomaly on the surface (e.g., Thatcher and England 1998; Leloup et al. 1999; Takeuchi and Fialko 2012). A large temperature anomaly can result in a weak zone with low seismic velocity that can be observed as a heterogeneous velocity structure in the seismic tomography data (Wittlinger et al. 1998). Furthermore, mylonite outcrops of exhumed faults (White et al. 1980) provide direct evidence for the existence of ductile shear zones in the lower crust under interplate (e.g., Rutter 1999; Little et al. 2002)

*Correspondence: zhang@seis.nagoya-u.ac.jp
[1] Graduate School of Environmental Studies, Nagoya University, Nagoya, Japan
Full list of author information is available at the end of the article

and intraplate faults (e.g., Shimada et al. 2004; Fusseis et al. 2006; Takahashi 2015).

Compared with interplate faults, intraplate strike-slip faults have much smaller slip rates, at <1 mm/year, and their age is much younger in the Japanese Islands (less than 3 Myr; Doke et al. 2012). However, heterogeneous structures beneath intraplate strike-slip faults observed by seismic tomography (e.g., Nakajima and Hasegawa 2007; Nakajima et al. 2010) and magnetotelluric survey (e.g., Ogawa and Honkura 2004; Yoshimura et al. 2009) suggest the existence of localized weak zones in the lower crust just below intraplate active faults (Iio et al. 2002, 2004). The spatial resolution of these observations is insufficient to resolve the structures of such ductile shear zones. Therefore, understanding the mechanisms that lead to shear strain concentration in the lower crust beneath an intraplate strike-slip is an important step in understanding the deformation of the crust.

In this study, we construct a series of numerical models on the deformation in the lower crust below an active intraplate strike-slip fault based on laboratory-derived rheological laws. We simulate the evolution of viscosity and deformation patterns of the lower crust beneath an immature intraplate strike-slip fault on a geological timescale. We consider three mechanisms of strain localization: shear and fault frictional heating, grain size reduction, and power-law creep. The effect of water is quantitatively evaluated with water fugacity. We discuss the role of shear strain concentration mechanisms and boundary conditions in the development of the shear zone. In addition, we compare the shear zones beneath intraplate and interplate strike-slip faults to identify the controlling factors for lower crustal shear localization under intraplate strike-slip faults.

Model description

We simulated the deformation of the lower crust beneath an intraplate strike-slip fault by applying a velocity boundary condition representing far-field loading. We solved the stress equilibrium equation and the heat flow equation for a thermo-mechanical coupled model, and we used laboratory-derived rheological laws to control the behavior of rocks.

Model geometry

The model domain is 35 km thick in the vertical (z) direction and 30 km wide in the fault-normal (x) direction. The Mohorovičić (Moho) discontinuity is represented by a horizontal boundary at a depth of 35 km. Following Thatcher and England (1998), we considered the problem in a 2-D plane perpendicular to the fault trace, as shown in Fig. 1. We assumed two layers: a rigid upper crust and a ductile lower crust, and the entire crust is composed of wet or dry anorthite. In the upper crust where brittle failure is the dominant mode of deformation, an infinitely long vertical creeping fault is assumed with the fault strike parallel to the y-axis. The lower crust is deformed by plastic flow, and there is a semi-brittle regime between the upper and the lower crust. The lower boundary of the semi-brittle regime is the brittle–ductile transition (BDT), the depth of which depends on the assumption of crustal rheology (Table 1). Considering the symmetry of the vertical strike-slip fault, our model region includes only one side of the fault bounded by the surface and a vertical plane of bilateral symmetry, which is taken to be the center of the shear zone.

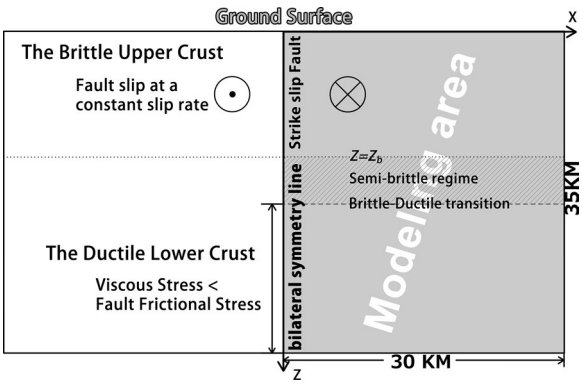

Fig. 1 Model geometry

Rheology

The constitutive relation for the plastic flow of rocks is described as follows (e.g., Bürgmann and Dresen 2008):

$$\dot{\varepsilon} = A\tau_s^n L^{-m} f_{H_2O}^r \exp\left(-\frac{Q+pV}{RT}\right), \quad (1)$$

Table 1 Model configurations

Model	Crustal rheology	Fault type	Grain size
W1C	Wet anorthite	Intraplate strike-slip fault	Constant ($L = 500$ μm)
D1C	Dry anorthite	Intraplate strike-slip fault	Constant ($L = 500$ μm)
W30C	Wet anorthite	Interplate strike-slip fault	Constant ($L = 500$ μm)
W1E	Wet anorthite	Intraplate strike-slip fault	Equilibrium
D1E	Dry anorthite	Intraplate strike-slip fault	Equilibrium
W30E	Wet anorthite	Interplate strike-slip fault	Equilibrium

Six model configurations were tested by this study. The rheological parameters for anorthite are summarized in Table 2. The nomenclature of the model configuration is as follows: The first letter denotes water content (D, dry; W, wet), and the last letter denotes grain size (C, constant; E, equilibrium). The number between two letters denotes the total relative velocity in mm/year

where τ_s is the maximum shear stress given by the square root of the second deviatoric stress invariant. L is the grain size. f_{H_2O} is water fugacity. Q and V are activation energy and activation volume, respectively. R is the universal gas constant. p is pressure, and A, n, m, r are material constants. The laboratory-derived parameters for anorthite are summarized in Table 2. Regarding the physical mechanism of plastic flow, in this study, we considered both diffusion creep and dislocation creep. For a given mineral, we assume that the same shear stress controls the two deformation mechanisms (e.g., Gueydan et al. 2001; Montési and Hirth 2003). Under this assumption, the total strain rate $\dot{\varepsilon}_{\text{total}}$ is expressed as the sum of the diffusion creep strain rate $\dot{\varepsilon}_{\text{diff}}$ and the strain rate caused by dislocation creep $\dot{\varepsilon}_{\text{disl}}$.

$$\dot{\varepsilon}_{\text{total}} = \dot{\varepsilon}_{\text{diff}} + \dot{\varepsilon}_{\text{disl}} \tag{2}$$

One can define the effective viscosity, such that

$$\eta_{\text{eff}} = \frac{\tau_s}{\dot{\varepsilon}_{\text{total}}}. \tag{3}$$

The grain size in this study is assumed following the model proposed by Bresser et al. (1998), who argued that grain growth occurs in the diffusion creep regime to increase the grain size to a size sufficient for dislocation creep to occur and dynamic recrystallization in dislocation creep regime leads to a grain size small enough for diffusion creep to occur. They postulated that the grain size is determined by the equation for Equilibrium Grain Size (L_{EGS}):

$$\dot{\varepsilon}_{\text{diff}}(T, p, \tau, L) = \dot{\varepsilon}_{\text{disl}}(T, p, \tau) \tag{4}$$

where T is temperature, p is pressure,τ is shear stress, and L is grain size. Combining Eqs. 1 and 4, we can obtain the expression for L_{EGS}, which is a function of temperature and shear stress:

$$L_{\text{EGS}} = \left[\frac{A_{\text{diff}}}{A_{\text{disl}}\tau_s^{n_{\text{disl}}-1}}\exp\left(\frac{Q_{\text{disl}} + pV_{\text{disl}} - Q_{\text{diff}} - pV_{\text{diff}}}{RT}\right)\right]^{\frac{1}{m_{\text{diff}}}} \tag{5}$$

The subscript diff and disl refer to the rheological parameters for diffusion creep and dislocation creep in Table 2.

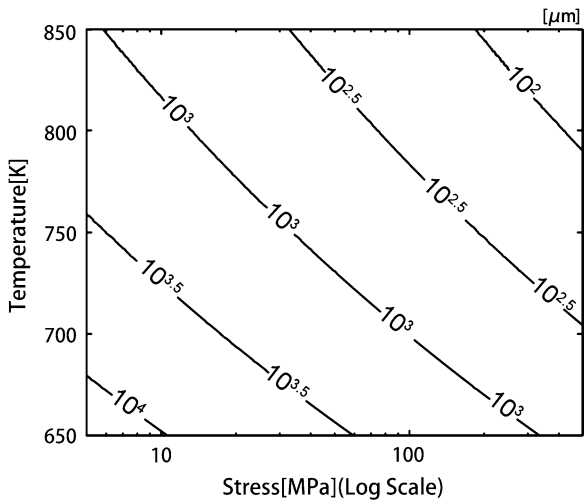

Fig. 2 Contours of equilibrium grain size as a function of temperature and stress, assuming wet anorthite rheology

From this assumption, we expect a large variation in grain size under the thermal and stress conditions of the lower crust (Fig. 2). We also tested a case of a Constant Grain Size (L_{CGS}) of 500 μm for comparison.

For wet rheology ($r = 1$), the effect of water weakening is evaluated with water fugacity f_{H_2O}. The fugacity of a gaseous species at any temperature (T) and pressure (p) can be calculated from the equation of state using the following equation (Karato 2012):

$$\log\frac{f(p,T)}{p} = \frac{1}{RT}\lim_{p_0\to 0}\int_{p_0}^{p}\left(V_{\text{m}}(p',T) - V_{\text{m}}^{\text{id}}(p',T)\right)dp'. \tag{6}$$

where V_{m} and V_{m}^{id} is molar volume of an real gas and an ideal gas, respectively. For real gas, we use van der Waals equation of state: $p = \frac{RT}{V_{\text{m}} - b} - \frac{a}{V_{\text{m}}^2}$. The van der Waals constants a and b of water (H_2O) are $5.537 \times 10^{-1}\text{m}^6\,\text{Pa}\,\text{mol}^{-2}$ and $3.049 \times 10^{-5}\text{m}^3\,\text{mol}^{-1}$, respectively. V_{m} in term $\frac{a}{V_m^2}$ can be approximated

Table 2 Rheological properties of rocks from laboratory measurements (Rybacki et al. 2006)

Anorthite	log*A* ($\text{MPa}^{-n-r}\mu\text{m}^m\,\text{s}^{-1}$)	*n* ($\text{MPa}^{-n-r}\mu\text{m}^m\,\text{s}^{-1}$)	*Q* (kJ/mol)	*m*	*r*	*V* (cm^3/mol)
Wet						
diff.[a]	−0.7	1	159	3	1	38
disl.[a]	0.2	3	345	0	1	38
Dry						
diff.[a]	12.1	1	460	3	0	24
disl.[a]	12.7	3	641	0	0	24

[a] diff. denotes diffusion creep, and disl. denotes dislocation creep

as $\frac{RT}{p}$ as ideal gas. Then, V_m can be calculated as $V_\mathrm{m} = \frac{R^3T^3}{pR^2T^2 + ap^2} + b$. Integrating Eq. 6 using the equation of state for real gas and ideal gas and substitute p and p_0 for p'. Let $p_0 = 0$, one obtains the expression for fugacity,

$$f(p,T) = \frac{pR^2T^2}{R^2T^2 + \mathrm{ap}} \exp\left(\frac{bp}{RT}\right). \tag{7}$$

Initial and boundary conditions

Because we consider an infinitely long strike-slip fault that cuts through the entire upper crust and terminates in the lower crust, there is no vertical motion. Far-field horizontal velocity v_0 is half of the total relative velocity. v_0 is assumed to be 0.5 and 15 mm/year for intraplate and interplate faults, respectively, and it is applied from surface to the depth of z_b and on the far-field boundaries. We assume the fault strength in the brittle fracture regime on the basis of Byerlee's law (Byerlee 1978):

$$\tau_f = \begin{cases} 0.85\sigma_\mathrm{n} & (\sigma_\mathrm{n} < 200\,[\mathrm{MPa}]) \\ 50 + 0.6\sigma_\mathrm{n} & (200\,[\mathrm{MPa}] < \sigma_\mathrm{n} < 1700\,[\mathrm{MPa}]), \end{cases} \tag{8}$$

where τ_f is frictional strength and σ_n is normal stress. The strength of a material in the plastic flow regime is highly sensitive to temperature, as shown in Eq. 1. In this model, we assume that the brittle fracture and plastic flow occur independently; as a result, the mechanism that gives a lower strength becomes the dominant mechanism of deformation. The transition conditions for brittle fracture to plastic flow (brittle–ductile transition, BDT) are given by

$$\tau_{yx} = \frac{1}{2}\eta_\mathrm{eff}\frac{\partial v}{\partial x} = \tau_\mathrm{f}. \tag{9}$$

Shear stress τ_{yx} is solved from the model of plastic flow using different model configurations (Table 1), and τ_f is the fault frictional strength. The shear strain rate ($\dot{\varepsilon}_{yx}$) is solved from Eq. 9. At the depth shallower than the depth of BDT, we apply stress boundary condition on the fault that the flow stress is equal to the fault frictional strength (Fig. 3b). The fault gradually terminates as slip decreases with depth. At the depth of BDT, the slip rate is 0. Slip rate at semi-brittle regime can be calculated by the integral of the shear strain rate ($\dot{\varepsilon}_{yx}$) over the entire domain in the x-direction. At depths greater than the BDT, no brittle fracture occurs, and the deformation is fully plastic. The velocity on the vertical plane of bilateral symmetry is zero. On the crust/mantle boundary, the boundary condition is $\mathrm{d}v/\mathrm{d}z = 0$.

The initial temperature is assumed with a uniform thermal gradient of 25 K/km (Table 3). The temperature of the Earth's surface is fixed to 0 °C. Zero heat flux at the vertical boundaries and a constant heat flux (0.065 W m^{-2}) at the Moho is assumed.

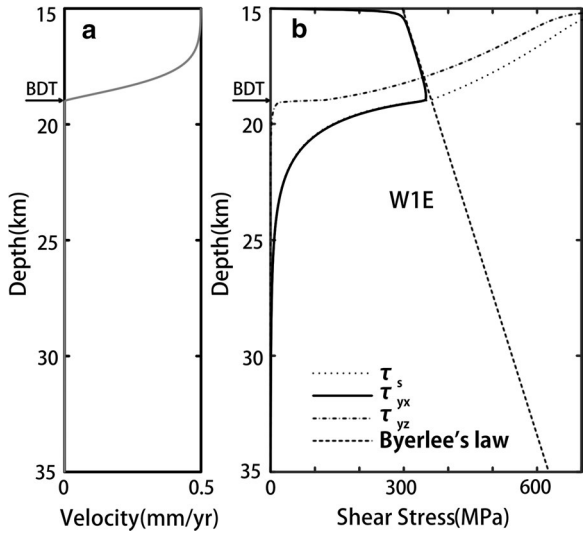

Fig. 3 **a** Fault slip velocity (v) and **b** shear stress on the bilateral symmetry line in the lower crust for model W1E. τ_s is the second deviatoric stress invariant; τ_{yx} and τ_{yz} are the yx and yz components of shear stress, respectively; and the *straight broken line* is based on Byerlee's law. The depth of the BDT is shown by *black arrows*

Table 3 Thermal and mechanical parameters

Parameter name	Abbr.	Value	Unit
Thermal parameters			
Thermal conductivity	k	2.60	W K^{-1} m^{-1}
Heat capacity	C_p	1130	J kg^{-1} K^{-1}
Geothermal gradient	$\frac{\mathrm{d}T}{\mathrm{d}z}$	25	K km^{-1}
Mechanical parameters			
Slip rate	v_0	0.5 or 15	mm year^{-1}
Crustal rock density	ρ	2800	kg m^{-3}

Thermo-mechanical coupling model

In our model, all mechanical energy is dissipated in heat and represents a source term in the heat flow equation:

$$\rho C_\mathrm{p}\frac{\partial T}{\partial t} = k\left(\frac{\partial^2 T}{\partial x^2} + \frac{\partial^2 T}{\partial z^2}\right) + H_\mathrm{s} + H_\mathrm{f}, \tag{10}$$

where the change in temperature T is a summation of thermal diffusion (k is the thermal conductivity) and volumetric heat generated by shear heating (H_s) and frictional heating (H_f). ρ is the density, and C_p is the specific heat capacity at constant pressure. The heat produced by shear per unit time and volume is given by

$$H_s = \tau_{ij}\dot{\varepsilon}_{ij}. \quad (11)$$

The heat produced by friction is approximated by the volumetric heating on a column of the grid closest to the fault (Leloup et al. 1999):

$$H_f = \tau_f \frac{v_0}{\Delta x}, \quad (12)$$

where τ_f is the frictional resistance defined in Eq. 8 and Δx is the width along the x-axis of the considered unit cell. We solved the heat flow equation in a 2-D space perpendicular to the fault (Fig. 1). In each time step, we assumed that the velocity is constant in time, and we solved the stress equilibrium equation for the velocity field. Because motion is purely horizontal, the only nonzero components of the stress are τ_{yx} and τ_{yz}:

$$\frac{\partial \tau_{yx}}{\partial x} + \frac{\partial \tau_{yz}}{\partial z} = 0. \quad (13)$$

All numerical calculations in this study were performed by using MATLAB. We used the Partial Differential Equation Toolbox to solve the mechanical equations, and we used the Alternating Direction Implicit finite difference method to solve the heat flow equation. The calculations were performed on a grid containing 700×600 (420,000) cells, each of which is 50 m in both of its width and height directions. Although a finer grid could give a more accurate solution, the overall pattern of the solutions is insensitive to the chosen grid size, as confirmed by simulations using a finer grid with a half grid size. We simulated the fault slip and temperature evolution by using the adaptive time step (e.g., Thatcher and England 1998) controlled by the amount of heat production. We calculated the temperature rise during 3 Myr because the initiation ages of active faulting in the inland areas of Japan are mostly less than 3 Myr (Doke et al. 2012).

Results

Effective viscosity of a rock depends on several environmental conditions such as shear stress, grain size, and temperature. In this section, we present the calculation results of shear stress and grain size distribution obtained by applying a 1-D linear geothermal gradient to evaluate the effects of grain size and power-law rheology. Moreover, we show the temperature anomaly produced by shear and frictional heating and the effective viscosity distribution.

Shear stress

As shown in Fig. 3b, the shear stress τ_{yz} becomes very large (>700 MPa) around point $x = 0, z = z_b$. This is because the effective viscosity is extremely large in the semi-brittle regime and the elasticity of rock has not been considered in this study. As the depth increases, τ_{yz} quickly decreases. At the depth greater than the depth of BDT, τ_{yz} becomes negligible compared with τ_{yx}, and the maximum shear stress τ_s is nearly equal to τ_{yx}. Therefore, the distribution of maximum shear stress in the lower crust below the BDT is considered to be a result of far-field loading and we focus our discussion to the lower crust below BDT.

Figure 4 shows the distribution of the maximum shear stress in the lower crust for our 6 cases. The depth of the BDT is different in each case, as is shown by gray broken lines in Figure 4. Compared with the wet anorthite, the dry anorthite requires a higher temperature to cause plastic deformation. The brittle region extends deeper into the crust (28–29 km depth), and the BDT for the dry anorthite case is about 8 km deeper than the cases of wet anorthite. Therefore, z_b was set at a depth of 25 km for the model with dry anorthite. In the case of interplate strike-slip faults (Fig. 4c, f), the shear stress is only slightly larger, and the BDT is about 2 km deeper than that for intraplate cases (Fig. 4a, d). However, the slip rate of an interplate strike-slip fault is 30 times larger than that of an intraplate strike-slip fault. Therefore, the shear stress in the lower crust and the depth of the BDT is not sensitive to the fault slip rate. Shear stress concentrates around the down-dip extension of the fault. The largest shear stress is located at the depth of the BDT. Shear stress drops with depth and distance from the fault.

Grain size distribution

We calculated L_{EGS} by balancing the shear strain rate of diffusion creep and dislocation creep. As examples, L_{EGS} obtained by the model W1E and model D1E with an initial temperature field is shown in Fig. 5. Small grains are located in highly sheared region because both L_{EGS} and shear strain rate depend on temperature and shear stress (Eq. 5 and Fig. 4). In our models, the minimum grain sizes are located at the depth of BDT under the fault where shear stress becomes the largest, nearly equal to the frictional strength of the fault. In models W1E and D1E, the minimum grain sizes are ~215 and ~17 μm at temperatures of ~475 and ~700 °C, respectively. The results of grain size measurements show that the plagioclase grains in ultramylonites have a mean diameter of 16 (Okudaira et al. 2015) and 85 μm (Okudaira et al. 2017) under the condition of ~700 and ~600 °C, respectively. Although our results of EGS are in agreement with these observations, comparison of the calculated results with the field observations is not straightforward. For example, the shear stress on the fault could be smaller than that estimated from Byerlee's law (Iio 1997). Also, even with the same temperature and stress conditions, dynamically recrystallized grain size may be still larger than L_{EGS} (Bresser et al. 2001).

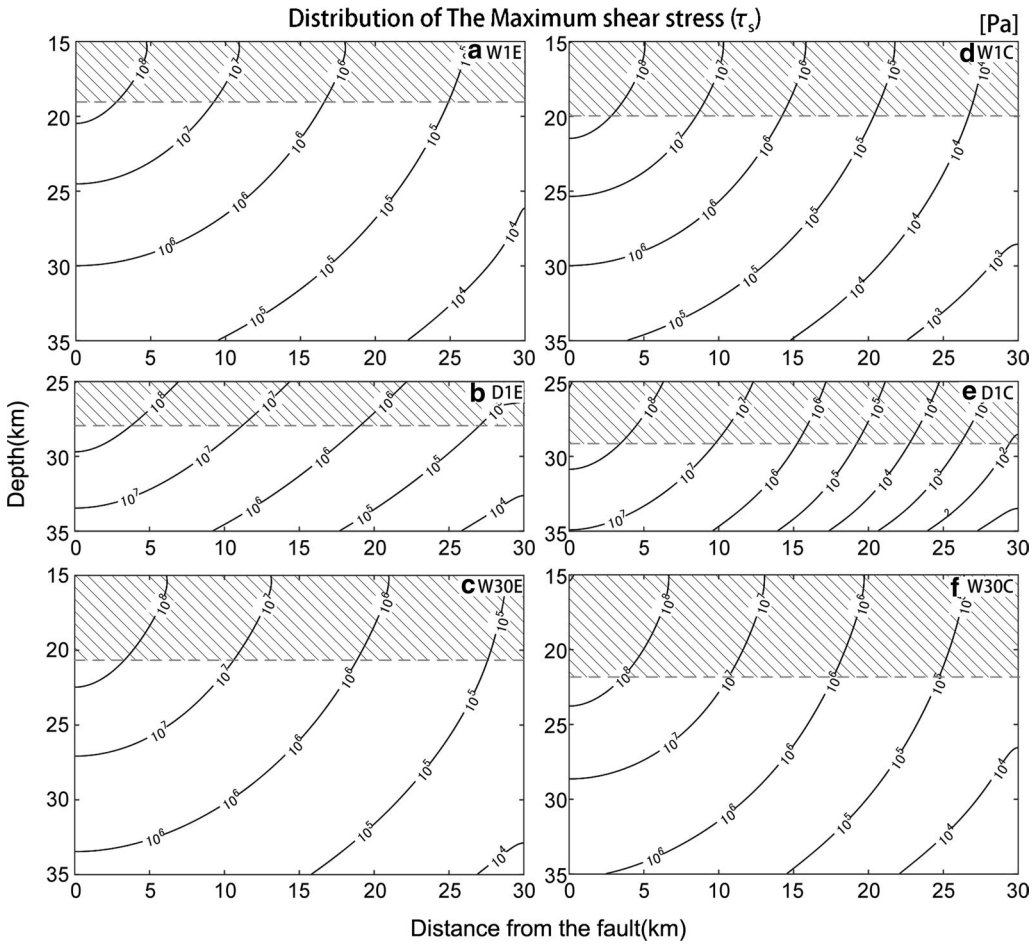

Fig. 4 Contours of shear stress (τ_s) in the lower crust as a function of depth and distance from the fault for models **a** W1E, **b** D1E, **c** W30E, **d** W1C, **e** D1C, and **f** W30C. The thickness of the lower crust and the depth of the BDT are dependent on the assumed rheology and far-field velocity (v_0). The *gray broken lines* represent the BDT depth

Outside the narrow mylonite zone, materials composed of relatively coarse grain size (up to few centimeters) are widely exposed over wide area (e.g., Markl 1998). Our calculation with EGS provides a fairly reasonable grain size distribution. However, in the far field where both temperature and shear stress is low, calculated L_{EGS} reaches several tens of centimeters, which is not realistic. This result may be ascribed to our assumptions of instantaneous grain growth following the equation for L_{EGS}. The mechanisms that limit grain size, such as the Zener pinning effect (e.g., Hillert 1988; Rohrer 2010), are not considered in this study.

Shear and frictional heating

Figure 6 shows temperature anomalies of 3 Myr after shearing and fault sliding were initiated. Assuming wet anorthite rheology for the lower crust, the maximum temperature increases for models W1E and W30E are about 15 and 219 K, respectively. The temperature increase for the case of an intraplate strike-slip fault is much lower than that for an interplate strike-slip fault. The temperature change is largely affected by frictional heating. Temperature rise creates a peak of heat flow anomaly on the fault trace. For an interplate strike-slip fault, the peak heat flow anomaly is ~55 mW/m^2 above the background heat flow which is 65 mW/m^2 (Fig. 7b). On the contrary, for an intraplate strike-slip fault, the expected heat flow anomaly is very small, less than 5% of the background value. Therefore, we cannot expect to detect a heat flow anomaly for the intraplate case (Tanaka et al. 2004). To illustrate how rock rheology affects the temperature increase, we also performed a calculation using dry anorthite (strong rheology). Figure 6b shows that the maximum temperature increase for the D1E model is about 22 K, which is higher than that for the wet

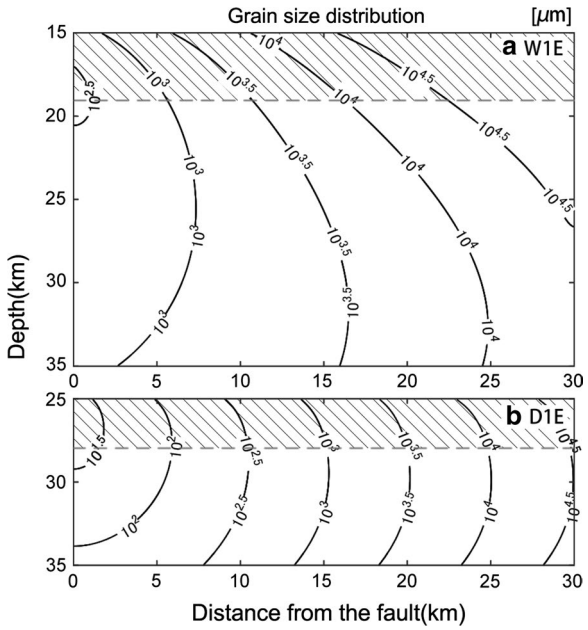

Fig. 5 Contours of equilibrium grain size distribution as a function of depth and distance from the fault, calculated from model W1E (**a**) and D1E (**b**). The *gray broken line* represents the BDT depth

anorthite case but still insufficient for causing an observable heat flow anomaly at the surface.

Effective viscosity

The effective viscosity structure strongly depends on assumptions applied for calculation, as shown in Fig. 8. For intraplate cases, the effective viscosity is about $10^{22.5}$ Pa s at the BDT under the fault. For the interplate case, in which the shear strain rate and shear stress are higher than those in the intraplate cases, the effective viscosity (Fig. 8c) becomes as small as about 10^{21}Pa s at the BDT under the fault.

The effective viscosity of dislocation creep is extremely high when stress is relatively small. In models assuming EGS, dislocation creep and diffusion creep had the same effective viscosity in our calculation. The effective viscosity at the far field and at the top of the lower crust is larger than 10^{25} Pa s because of the relatively low temperature and small stress. In these regions, rocks behave like a rigid body.

On the other hand, in models assuming CGS, diffusion creep becomes the dominate deformation mechanism where stress is relatively small. Owing to the linear geothermal gradient, the effective viscosity has a layered structure in the far field. In the shear zone where the stress is large, dislocation creep dominates. The broken lines in Fig. 8d–f show the location in which dislocation creep and diffusion creep with a grain size of 500 μm have equal contribution. Dislocation creep dominates on the left side, and diffusion creep dominates on the right side of the broken line.

A comparison of wet and dry anorthite shows that the effective viscosity is significantly lowered by the present of water, whereas in previous studies of interplate strike-slip faults (e.g., Takeuchi and Fialko 2013; Moore and Parsons 2015), due to the elevated temperature field, the effective viscosity for wet and dry rheologies has similar magnitude in the center of the shear zone. This is not the case in the intraplate strike-slip fault, because change in effective viscosity structure due to shear and frictional heating is negligible.

Discussion

In this section, we discuss the relative importance of candidate mechanisms for the formation and maintenance of the shear zone in the lower crust beneath an intraplate strike-slip fault.

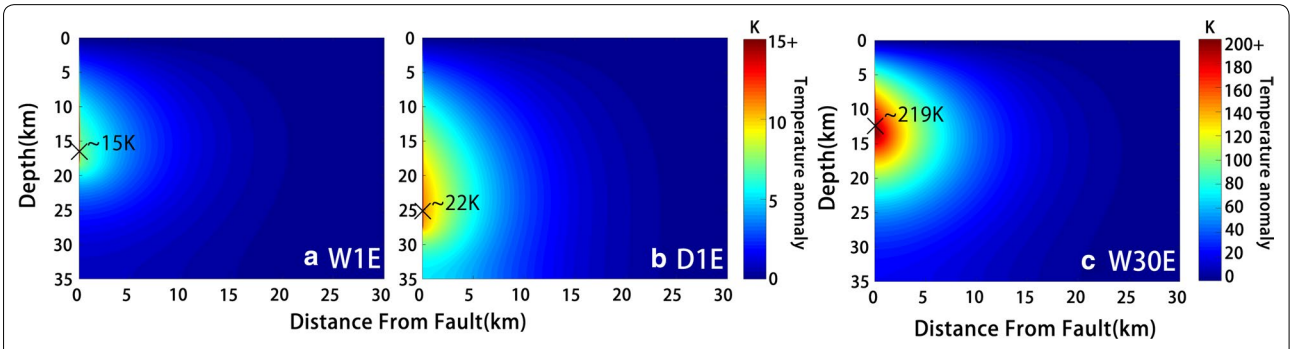

Fig. 6 Temperature anomaly produced by shear and frictional heating versus depth and distance from the fault for models **a** W1E, **b** D1E and **c** W30E after 3 Myr of fault sliding. "×" shows the location of maximum temperature increase; *numbers* indicate the magnitude of maximum temperature increase

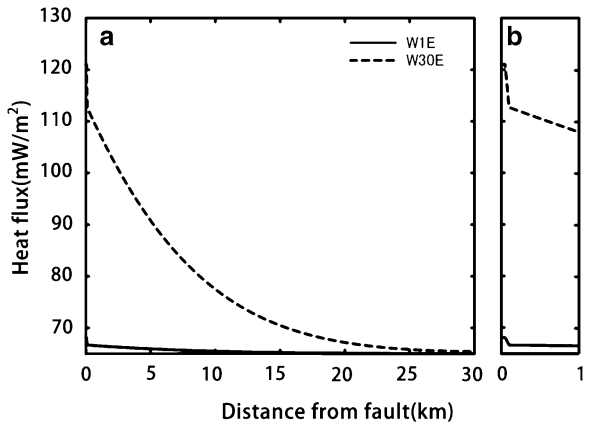

Fig. 7 **a** Surface heat flow for simulation of interplate (*broken line*) and intraplate (*solid line*) strike-slip faults. **b** Enlarged view of the fault core, the *sharp peak* above the fault ($x = \sim 0$) was created by fault frictional heating

Shear, as well as frictional heating, has been considered as a main cause of the lower crustal shear zone beneath a fault and the associated heat flow anomaly for interplate strike-slip faults such as the San Andreas Fault (e.g., Lachenbruch and Sass 1980; Leloup et al. 1999). We compared the shear strain rate obtained from a temperature field of 3 Myr (solid line in Fig. 9) and that obtained from an initial temperature field (broken line in Fig. 9). For the interplate strike-slip fault, a significant increase in temperature occurred around the fault tip at a depth of about 12 km (Fig. 6c). Our result of temperature increase in model W30E is consistent with the results of recent thermo-mechanical models of interplate strike-slip faults (e.g., Takeuchi and Fialko 2012; Moore and Parsons 2015). The maximum temperature increase in the cases of wet rheologies is ~200 °C, and the effective viscosity was significantly lowered by the increased temperature. A comparison with the shear strain rate with the 1-D linear geothermal gradient revealed that the shear zone became narrower and the depth of BDT became shallower (Fig. 9b) after temperature is increased, which indicates that the depths of BDT for interplate strike-slip faults are time dependent.

On the contrary, for the case of the intraplate strike-slip fault (Fig. 9a), the shear strain rate change during 3 Myr was negligible because the temperature increase was minimal (~20 /650 K). So shear and frictional heating on long-term (geological time scale) thermal structures is negligible for intraplate strike-slip faults. We conclude that such heating is not the main cause of the formation of shear zone under intraplate faults.

The amount of heat generated by shear and frictional heating can be increased by the absence of water. In the previous studies (e.g., Takeuchi and Fialko 2012; Moore and Parsons 2015), the temperature increase in the cases of dry rheologies is about 200 °C higher than that in the cases of wet rheologies. In our study, the effect of water on temperature increase is not significant because the maximum shear strain rate (Fig. 10) and shear stress (Fig. 4) is insensitive to the rock rheology. Instead, the depth increase in BDT due to the absence of water is ~8 km, which is equivalent to a temperature increase of ~200 °C.

In the current model, the degree of shear strain concentration was influenced by the assumption of rheology. Deformation was more localized in the cases of power-law fluid (Fig. 10a, b) than in the case of Newtonian fluid (Fig. 10c). A comparison of the results of models W1E and W1C revealed that shear strain rate distributions are similar in the shear zone, implying that in the current study, the assumption of grain size dose not affect shear strain concentration. Therefore, weakening due to power-law rheology is the most important mechanism in the formation of the shear zone in the lower crust. However, it should be noted that we only consider diffusion creep as a grain size dependent creep in this study. In the fine grained mylonites, deformation mechanisms other than diffusion creep, such as grain boundary sliding (Boullier and Gueguen 1975; White 1979) could occur to further reduce the strength of rocks and enhance shear strain localization.

Once a shear zone has been formed in the lower crust, the strength heterogeneity produced by the material with small grain sizes will remain over a geological time scale (~10^8 years, Tullis and Yund 1982). Commonly observed mylonite near exhumed shear zones (White et al. 1980) shows evidence for these long-lived weak zones beneath intraplate faults. Thus, lower shear strengths are maintained by materials with small grain sizes and strain localization should be a common feature for many active faults.

In the far field, although the shear strain rate in the W1C model was larger than that in W1E, the shear stress in the cases of CGS is smaller than that for the cases of EGS because the effective viscosity is significantly lowered by the diffusion creep. Because the shear strain rate in the far field is much smaller than that in the shear zone, the deformation in the far field has almost no influence on the deformation in the localized shear zone.

A simplifying assumption in our calculation is that EGS is achieved instantaneously, which may not be realistic. According to the model of Bresser et al. (1998), grain size evolves toward EGS depending on the strain rate at each

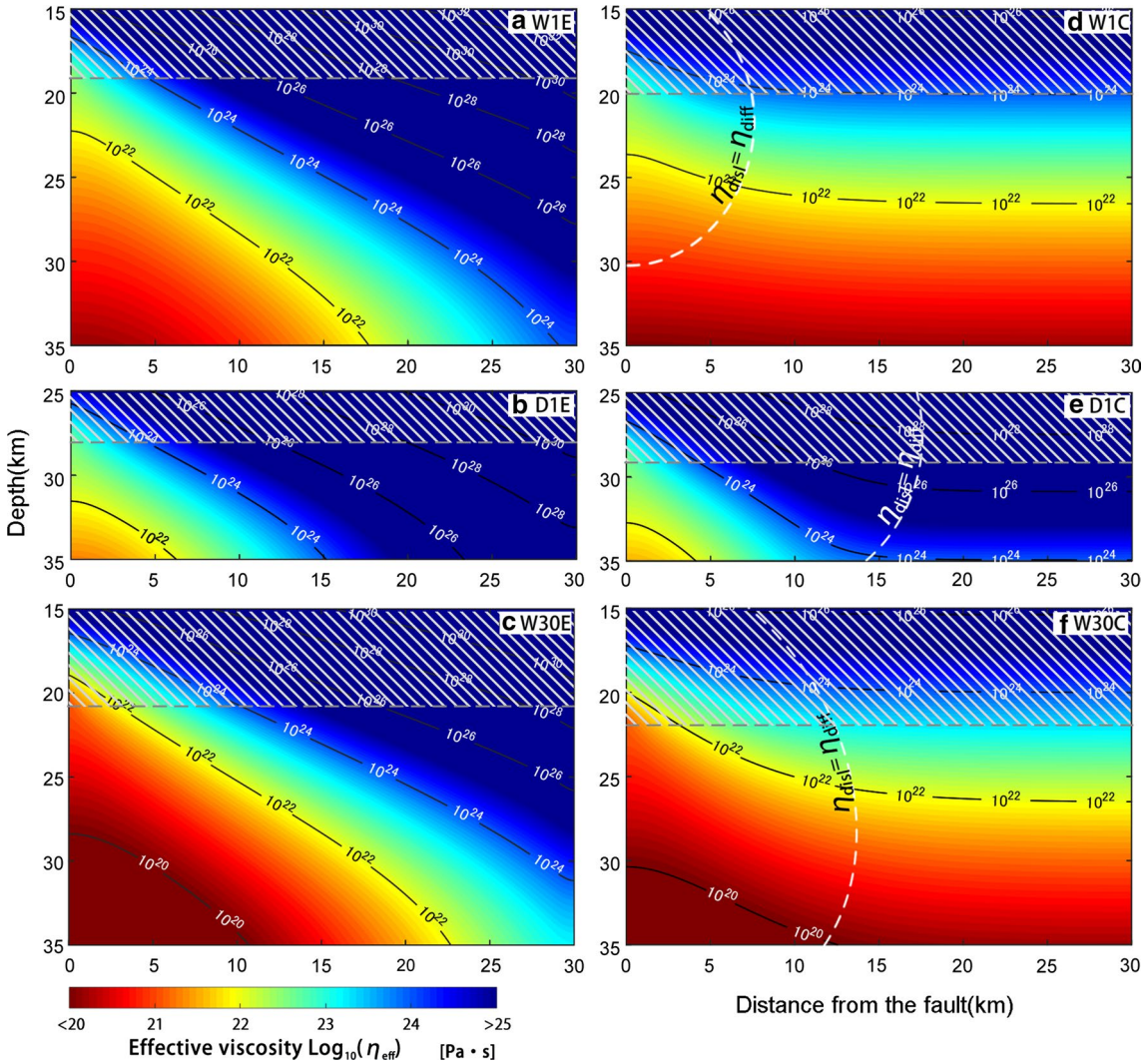

Fig. 8 Effective viscosity versus depth and distance from the fault for equilibrium grain size (**a**–**c**) and constant grain size (**d**–**f**). The *white broken line* in **d**–**f** indicates the location in which diffusion creep and dislocation creep have the same slip rate

location. Since the strain rate distribution in our calculation does not significantly change with time, the resulting EGS can be considered as the result of long-term steady-state deformation. Our results demonstrate that a relative motion across an intraplate fault, no matter how slow it moves, can create characteristic grain size distribution and corresponding strain localization in the lower crust. The model also predicts that lower crustal rocks in the far field should be like a rigid body. Studies of post-seismic deformation showed that plastic flow in the lower crust after the 1992 Landers and 1999 Hector Mine earthquakes was not significant (Pollitz 2001; Freed et al. 2007). Our result of the effective viscosity structure with the EGS assumption is in good agreement with such observation because in that case, the plastic deformation is limited in a narrow shear zone under the fault.

For interplate strike-slip faults, Savage and Burford (1973) proposed a kinematic model with a buried dislocation in an elastic half-space; this model has been used to explain geodetically observed interseismic strain accumulation. For intraplate strike-slip faults, a similar dislocation model has been applied and yielded a reasonable estimate of the fault-locking depth (e.g., Ohzono et al. 2011). The current model demonstrates that such a localized shear zone appears even in an intraplate case with a very low slip rate. This provides a physical basis for applicability of the Savage and Burford (1973) model to intraplate strike-slip faults.

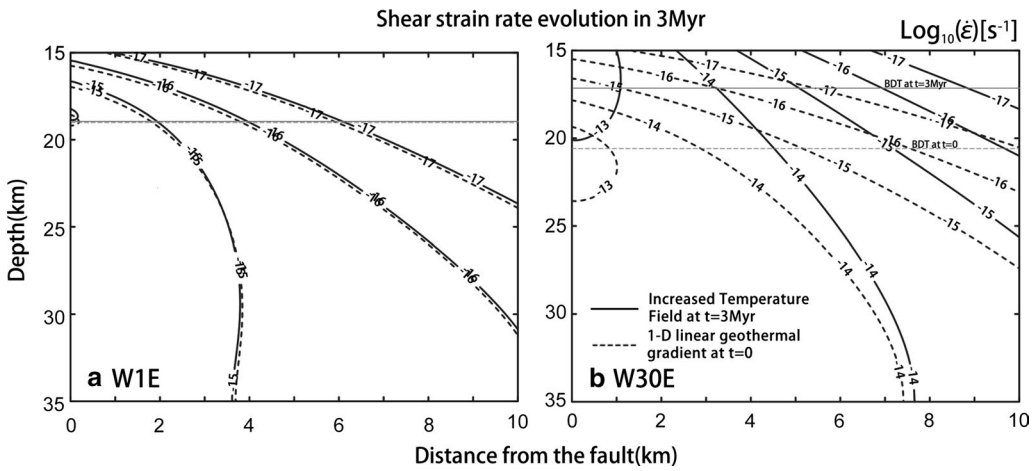

Fig. 9 Shear strain rate changed by increased temperature for **a** W1E and **b** W30E. The *broken contour lines* show the shear strain rate with the temperature field of a 1-D geothermal gradient, and the *solid contour lines* show the shear strain rate with the temperature field from a 3 Myr simulation. *Gray broken lines* and *solid lines* represent the BDT depth at $t = 0$ and at $t = 3$Myr, respectively

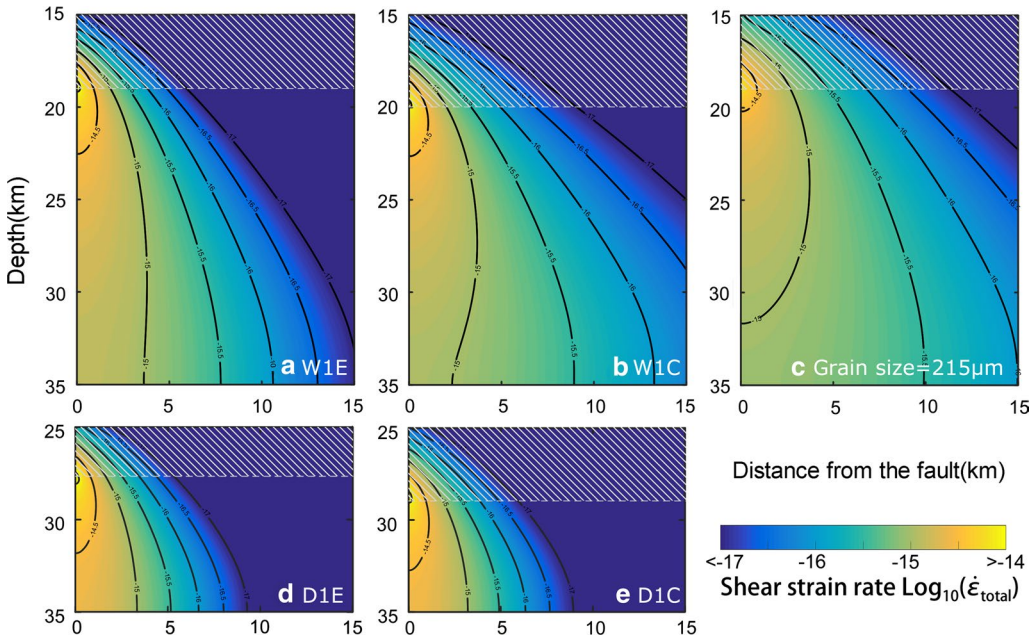

Fig. 10 Shear strain rate for models **a** W1E, **b** W1C, **d** D1E and **e** D1C. **c** Linear model deformed by diffusion creep has a constant grain size of 215 μm (minimum grain size of model W1E)

Conclusion

We have considered the formation and maintenance of the shear zone under an intraplate strike-slip fault. Models that incorporate laboratory-derived temperature-dependent power-law rheology, grain size, and shear and frictional heating are examined to understand the mechanism and boundary conditions that influence the deformation of the lower crust. Water is very important to reduce the temperature requirement for plastic deformation in the lower crust, as for wet anorthite, deformation is fully plastic at temperature of ~475 °C, whereas for dry anorthite is ~700 °C. The temperature anomaly owing to 3 Myr of heat generation on an intraplate strike-slip fault is negligibly small. In our model, dynamically recrystallized materials with small grain sizes are important for maintaining a shear zone on a geological time scale of $\sim 10^8$ years. The

degree of shear strain concentration is controlled by the weakening effect due to nonlinear relation between shear strain rate and stress (power-law rheology).

Abbreviations
BDT: brittle–ductile transition; diff.: diffusion creep; disl.: dislocation creep; EGS: equilibrium grain size; CGS: constant grain size.

Authors' contributions
XZ constructed the numerical model for the study, conducted all numerical experiments and drafted the manuscript. TS conceived of the study, participated in its design and coordination and helped to draft the manuscript. Both authors read and approved the final manuscript.

Author details
[1] Graduate School of Environmental Studies, Nagoya University, Nagoya, Japan. [2] Disaster Mitigation Research Center, Nagoya University, Nagoya, Japan.

Acknowledgements
The authors would like to thank T. Ito and R. Sasajima for providing kind supervision, helpful comments, and continued support. Constructive reviews by J. Muto, T. Okudaira, and an anonymous reviewer improved the manuscript. This study was supported by JSPS KAKENHI Grant Number 261090003. The corresponding author was supported by a Japanese Government Scholarship for his study in Japan.

Competing interests
The authors declare that they have no competing interests.

Publisher's Note

Received: 5 February 2017 Accepted: 8 June 2017
Published online: 19 June 2017

References
Boullier A, Gueguen Y (1975) Sp-mylonites: origin of some mylonites by superplastic flow. Contrib Mineral Petrol 50(2):93–104
Bürgmann R, Dresen G (2008) Rheology of the lower crust and upper mantle: evidence from rock mechanics, geodesy, and field observations. Ann Rev Earth Planet Sci 36(1):531
Byerlee JD (1978) Friction of rocks. Pure Appl Geophys 116(4–5):615–626
De Bresser J, Peach C, Reijs J, Spiers C (1998) On dynamic recrystallization during solid state flow: effects of stress and temperature. Geophys Res Lett 25(18):3457–3460
De Bresser J, Ter Heege J, Spiers C (2001) Grain size reduction by dynamic recrystallization: Can it result in major rheological weakening? Int J Earth Sci 90(1):28–45
Doke R, Tanikawa S, Yasue K, Nakayasu A, Niizato T, Umeda K, Tanaka T (2012) Spatial patterns of initiation ages of active faulting in the Japanese Islands. Active Fault Res 37:1–15
Fleitout L, Froidevaux C (1980) Thermal and mechanical evolution of shear zones. J Struct Geol 2(1–2):159–164
Freed AM, Bürgmann R, Herring T (2007) Far-reaching transient motions after mojave earthquakes require broad mantle flow beneath a strong crust. Geophys Res Lett 34(19):L19302
Fusseis F, Handy M, Schrank C (2006) Networking of shear zones at the brittle-to-viscous transition (cap de creus, ne spain). J Struct Geol 28(7):1228–1243
Gueydan F, Leroy YM, Jolivet L (2001) Grain-size-sensitive flow and shear-stress enhancement at the brittle-ductile transition of the continental crust. Int J Earth Sci 90(1):181–196
Hillert M (1988) Inhibition of grain growth by second-phase particles. Acta Metall 36(12):3177–3181
Iio Y (1997) Frictional coefficient on faults in a seismogenic region inferred from earthquake mechanism solutions. J Geophys Res Solid Earth 102(B3):5403–5412
Iio Y, Sagiya T, Kobayashi Y, Shiozaki I (2002) Water-weakened lower crust and its role in the concentrated deformation in the Japanese Islands. Earth Planet Sci Lett 203(1):245–253
Iio Y, Sagiya T, Kobayashi Y (2004) Origin of the concentrated deformation zone in the japanese islands and stress accumulation process of intraplate earthquakes. Earth Planets Space 56(8):831–842
Karato S (2012) Deformation of earth materials. An introduction to the rheology of solid earth, Chap 212. Cambridge University Press, Cambridge
Lachenbruch AH, Sass J (1980) Heat flow and energetics of the San Andreas Fault Zone. J Geophys Res Solid Earth (1978–2012) 85(B11):6185–6222
Leloup PH, Ricard Y, Battaglia J, Lacassin R (1999) Shear heating in continental strike-slip shear zones: model and field examples. Geophys J Int 136(1):19–40
Little T, Holcombe R, Ilg B (2002) Kinematics of oblique collision and ramping inferred from microstructures and strain in middle crustal rocks, central Southern Alps, New Zealand. J Struct Geol 24(1):219–239
Markl G (1998) The Eidsfjord anorthosite, Vesterålen, Norway: field observations and geochemical data. Norges Geologiske Undersokelse 434:53–76
Montési LG, Hirth G (2003) Grain size evolution and the rheology of ductile shear zones: from laboratory experiments to postseismic creep. Earth Planet Sci Lett 211(1):97–110
Moore JD, Parsons B (2015) Scaling of viscous shear zones with depth-dependent viscosity and power-law stress–strain-rate dependence. Geophys J Int 202(1):242–260
Nakajima J, Hasegawa A (2007) Deep crustal structure along the Niigata–Kobe Tectonic Zone, Japan: its origin and segmentation. Earth Planets Space 59(2):e5
Nakajima J, Kato A, Iwasaki T, Ohmi S, Okada T, Takeda T et al (2010) Deep crustal structure around the Atotsugawa fault system, central Japan: a weak zone below the seismogenic zone and its role in earthquake generation. Earth Planets Space 62(7):555–566
Ogawa Y, Honkura Y (2004) Mid-crustal electrical conductors and their correlations to seismicity and deformation at Itoigawa–Shizuoka Tectonic Line, central Japan. Earth Planets Space 56(12):1285–1291
Ohzono M, Sagiya T, Hirahara K, Hashimoto M, Takeuchi A, Hoso Y, Wada Y, Onoue K, Ohya F, Doke R (2011) Strain accumulation process around the Atotsugawa fault system in the Niigata–Kobe Tectonic Zone, central Japan. Geophys J Int 184(3):977–990
Okudaira T, Jeřábek P, Stünitz H, Fusseis F (2015) High-temperature fracturing and subsequent grain-size-sensitive creep in lower crustal gabbros: Evidence for coseismic loading followed by creep during decaying stress in the lower crust? J Geophys Res Solid Earth 120(5):3119–3141
Okudaira T, Shigematsu N, Harigane Y, Yoshida K (2017) Grain size reduction due to fracturing and subsequent grain-size-sensitive creep in a lower crustal shear zone in the presence of a Co_2-bearing fluid. J Struct Geol 95:171–187. doi:10.1016/j.jsg.2016.11.001
Pollitz FF (2001) Viscoelastic shear zone model of a strike-slip earthquake cycle. J Geophys Res 106(26):526–541
Rohrer GS (2010) Introduction to grains, phases, and interfacesan interpretation of microstructure. Trans Aime, 1948, vol 175, pp 15–51, by cs smith. Metall Mater Trans A 41(5):1063–1100
Rutter E (1999) On the relationship between the formation of shear zones and the form of the flow law for rocks undergoing dynamic recrystallization. Tectonophysics 303(1):147–158
Rybacki E, Gottschalk M, Wirth R, Dresen G (2006) Influence of water fugacity and activation volume on the flow properties of fine-grained anorthite aggregates. J Geophys Res Solid Earth 111(B3):B03203
Savage J, Burford R (1973) Geodetic determination of relative plate motion in central California. J Geophys Res 78(5):832–845
Shimada K, Tanaka H, Toyoshima T, Obara T, Niizato T (2004) Occurrence of mylonite zones and pseudotachylyte veins around the base of the upper crust: An example from the southern Hidaka metamorphic belt, Samani area, Hokkaido, Japan. Earth Planets Space 56(12):1217–1223
Takahashi Y (2015) Geotectonic evolution of the Nihonkoku Mylonite Zone of north central Japan based on geology, geochemistry, and radiometric ages of the Nihonkoku Mylonites. In: Mukherjee S, Mulchrone KF (eds) Ductile shear zones: from micro- to macro-scales. Wiley, Chichester, UK

Takeuchi CS, Fialko Y (2012) Dynamic models of interseismic deformation and stress transfer from plate motion to continental transform faults. J Geophys Res Solid Earth 117(B5):B05403
Takeuchi CS, Fialko Y (2013) On the effects of thermally weakened ductile shear zones on postseismic deformation. J Geophys Res Solid Earth 118(12):6295–6310
Tanaka A, Yamano M, Yano Y, Sasada M (2004) Geothermal gradient and heat flow data in and around Japan (i): Appraisal of heat flow from geothermal gradient data. Earth Planets Space 56(12):1191–1194
Thatcher W, England PC (1998) Ductile shear zones beneath strike-slip faults: implications for the thermomechanics of the San Andreas Fault Zone. J Geophys Res Solid Earth 103(B1):891–905
Tullis J, Yund RA (1982) Grain growth kinetics of quartz and calcite aggregates. J Geol 90:301–318
White S (1979) Grain and sub-grain size variations across a mylonite zone. Contrib Mineral Petrol 70(2):193–202
White S, Burrows S, Carreras J, Shaw N, Humphreys F (1980) On mylonites in ductile shear zones. J Struct Geol 2(1–2):175–187
Wittlinger G, Tapponnier P, Poupinet G, Mei J, Danian S, Herquel G, Masson F (1998) Tomographic evidence for localized lithospheric shear along the Altyn Tagh fault. Science 282(5386):74–76
Yoshimura R, Oshiman N, Uyeshima M, Toh H, Uto T, Kanezaki H, Mochido Y, Aizawa K, Ogawa Y, Nishitani T et al (2009) Magnetotelluric transect across the Niigata-Kobe tectonic zone, central Japan: a clear correlation between strain accumulation and resistivity structure. Geophys Res Lett 36(20):L20311
Yuen D, Fleitout L, Schubert G, Froidevaux C (1978) Shear deformation zones along major transform faults and subducting slabs. Geophys J Int 54(1):93–119